ACS OMEGA

http://pubs.acs.org/journal/acsodf

Article

Band Structure Engineering and Defect Passivation of $Cu_xAg_{1-x}InS_2$/ZnS Quantum Dots to Enhance Photoelectrochemical Hydrogen Evolution

Heng Guo,* Peng Yang, Jie Hu, Anqiang Jiang, Haiyuan Chen,* Xiaobin Niu, and Ying Zhou

Cite This: *ACS Omega* 2022, 7, 9642−9651

Read Online

ACCESS | Metrics & More | Article Recommendations | Supporting Information

ABSTRACT: The $AgInS_2$ colloidal quantum dot (CQD) is a promising photoanode material with a relatively wide band gap for photoelectrochemical (PEC) solar-driven hydrogen (H_2) evolution. However, the unsuitable energy band structure still forms undesired energy barriers and leads to serious charge carrier recombination with low solar to hydrogen conversion efficiency. Here, we propose to use the ZnS shell for defect passivation and Cu ion doping for band structure engineering to design and synthesize a series of $Cu_xAg_{1-x}InS_2$/ZnS CQDs. ZnS shell-assisted defect passivation suppresses charge carrier recombination because of the formation of the core/shell heterojunction interface, enhancing the performance of PEC devices with better charge separation and stability. More importantly, the tunable Cu doping concentration in $AgInS_2$ CQDs leads to the shift of the quantum dot band alignment, which greatly promotes the interfacial charge separation and transfer. As a result, $Cu_xAg_{1-x}InS_2$/ZnS CQD photoanodes for PEC cells exhibit an enhanced photocurrent of 5.8 mA cm^{-2} at 0.8 V versus the RHE, showing excellent photoelectrocatalytic activity for H_2 production with greater chemical-/photostability.

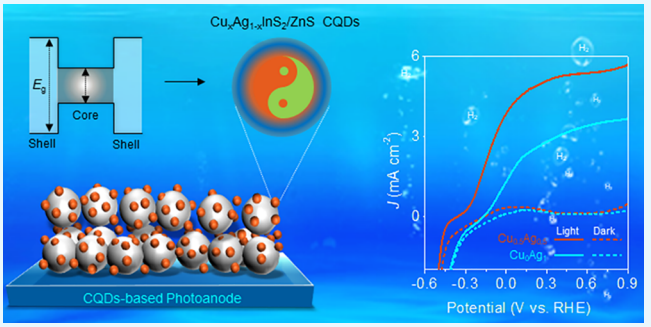

1. INTRODUCTION

Colloidal quantum dot (CQD) photoelectrochemical (PEC) cells have improved significantly in performance for hydrogen production over the past decade,[1,2] due to their excellent optoelectronic properties. The size-, structure-, and chemical-composition-dependent bandgap of CQDs provides an opportunity to harvest a wide solar spectrum up to the near-infrared (NIR) range.[3] This property makes CQDs attractive photosensitizer candidates for photoelectrode materials and allows for application in the visible and NIR-bandgap photovoltaic and optoelectronic devices,[4,5] such as solar cells,[6,7] photodetectors,[8,9] and light-emitting diodes (LEDs).[10−13] Moreover, multiple exciton generation in CQDs has the potential to greatly increase the utilization of the solar fluence and boost the solar-to-hydrogen (STH) conversion efficiency of CQD PEC cells.[14] Rapid progress in CQD PEC cells has been achieved by improvements in the PEC cell efficiency and stability. Energy band engineering, surface passivation, and device architecture optimization are three major requirements for improving light absorption and increasing charge collection, which further increases their promise.[15,16]

Generally, a typical glass|FTO|TiO_2|CQD-based photoanode (Figure 1a) for PEC cells displays a heterojunction with a suitable interfacial energy band alignment in a PEC cell configuration (Figure 1b). When irradiated by light, photo-generated exciton dissociation occurs at the CQD/TiO_2 heterogeneous interface, and the photogenerated electrons transfer into TiO_2 with a less negative conduction band (CB) and move to the metal counter electrode to conduct a H_2O reduction reaction for H_2 generation.[17,18] The photogenerated hole transfers to a less positive valence band (VB) via the contact interface and is further consumed by the S^{2-}/SO_3^{2-} scavenger in the electrolyte.[19] In previous reports, it is proved that the aforementioned efforts to improve the H_2 production performance are essential.[2,20] However, further advances still depend on the suitable electronic band structure, efficient charge transfer, and high photochemical stability of the core/shell CQD (Figure 1c) itself.

Band structure engineering, such as size/shape controlling, doping strategy, and chemical composition management have demonstrated enhanced electron-extraction efficiency in CQD PEC cells.[21] In CQDs, intentional electronic doping results in exchange charges with the CB and VB via radiative and nonradiative transitions, affecting the electric/optical proper-

Received: December 13, 2021
Accepted: February 14, 2022
Published: March 9, 2022

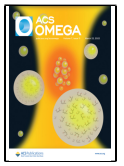

https://doi.org/10.1021/acsomega.1c07045
ACS Omega 2022, 7, 9642−9651

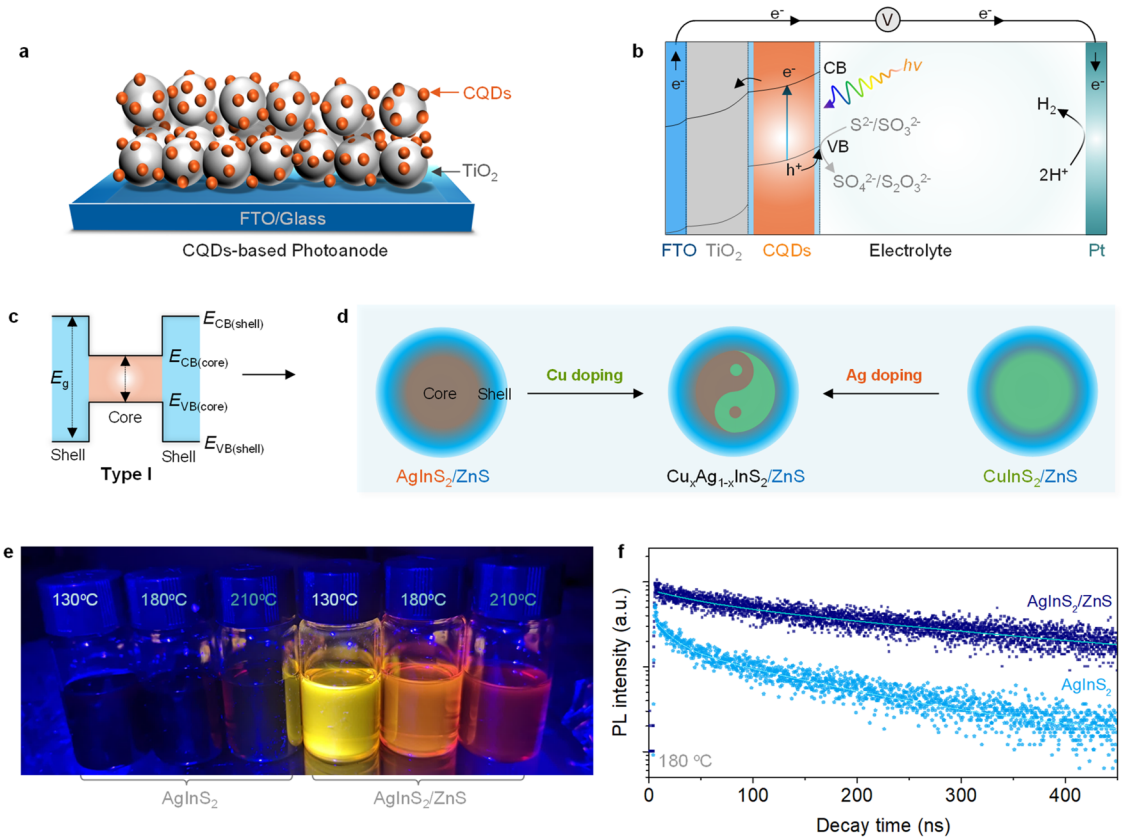

Figure 1. Manipulating the catalytic activity of photoanodes by modulating the structure of CQDs: (a) Schematic diagram for the CQD-based photoanode with the structure of glass|FTO|TiO_2|CQDs. (b) Figure and predictable band alignment of CQD-based photoanode photoelectrochemical cells. (c) Band structure of Type I CQDs. (d) Schematic illustration for band structure engineering and defect passivation of Cu-doped $AgInS_2$/ZnS CQDs. (e) The luminescence photograph of $AgInS_2$ and $AgInS_2$/ZnS CQDs synthesized at different reaction temperatures under UV lamp excitation at 325 nm. (f) Photoluminescence decay curves of $AgInS_2$ and $AgInS_2$/ZnS CQDs synthesized at 180 °C.

ties of host CQDs.[15,22] Significant improvements in electronic band alignment, luminescence excited-state lifetime, and quantum efficiency for CQDs have been achieved by the incorporation of aliovalent dopants such as Cu, Mn, and Ni.[23−25] Among those, Cu-doped CQDs have been well synthesized, as the various host CQDs progressed from heavy metal (Pb and Cd) to heavy metal free (I−III−VI: Cu, Ag, Zn, In, S).[26] The Cu doping in host CQDs is investigated extensively and derived from the Cu oxidation state, Cu-related emission, and its stability.[27] In an acceptable mechanism, Cu T_2 energy states between the CB and VB of host CQDs induce the elimination of the intrinsic band-edge emission of host CQDs, resulting in a broad and intense emission in a wide wavelength range with a much longer excited-state lifetime.[28,29]

However, the Cu-doping-related emission still suffers from the photostability problem, due to photooxidation.[30] The Cu-state-related emission is ascribed to the CB energy of host nanocrystals, arising from charge-transfer recombination of the $e^-_{CB} \rightarrow Cu^{2+}$, existing between Cu-localized holes and delocalized CB-like electrons.[31] Additionally, the large surface-to-volume ratio of the as-synthesized CQDs leads to the appearance of surface traps/defects, resulting in added opportunities for electronic defect formation. Shell-assisted defect passivation for Cu-doped CQDs is a proven effective approach to combat these losses. The overgrowth of a shell leads to surface passivation, heterojunction formation (e.g., type I heterojunction, Ohmic junction, and Schottkey junction), and photostability.[32,33] In core−shell CQD systems, the inorganic shell can reduce surface-related traps/defects by passivating the CQD surface. Ideally, the defect passivation has been carried out by a combination of doped CQDs and core/shell CQDs. The band structure engineering and defect passivation strategy will build the effective transmission path of the photoinduced carrier, which could have the potential to improve the CQD characteristics.

Here, we report a grown-doping strategy (Figure 1d) to design and synthesize a less toxic I−III−VI_2 group $AgInS_2$ (AIS) colloidal quantum dot with ZnS shell-assisted defect passivation. The insertion of a Cu dopant with high diffusivity in AIS CQD lattices regulates the energy band structure and photoluminescence spectra of $Cu_xAg_{1-x}InS_2$/ZnS CQDs with typelcore/shell heterojunction structure. The best substitution ratio is x = 0.5. The $Cu_{0.5}Ag_{0.5}InS_2$/ZnS CQDs show the optimized band alignment, tunable spectral region, and increased charge carrier lifetime. Moreover, the charge separation in the CQD/TiO_2 interface is efficiently enhanced by forming the heterojunction interface hindering the charge recombination. As expected, the PEC cells based on $Cu_{0.5}Ag_{0.5}InS_2$/ZnS CQDs exhibit a saturated photocurrent density of 5.8 mA cm^{-2} with good stability toward solar-driven H_2 production. This work opens a new avenue for heavy metal-free $Cu_xAg_{1-x}InS_2$/ZnS CQDs as efficient photoelectrocatalysts to hydrogen generation.

https://doi.org/10.1021/acsomega.1c07045
ACS Omega 2022, 7, 9642−9651

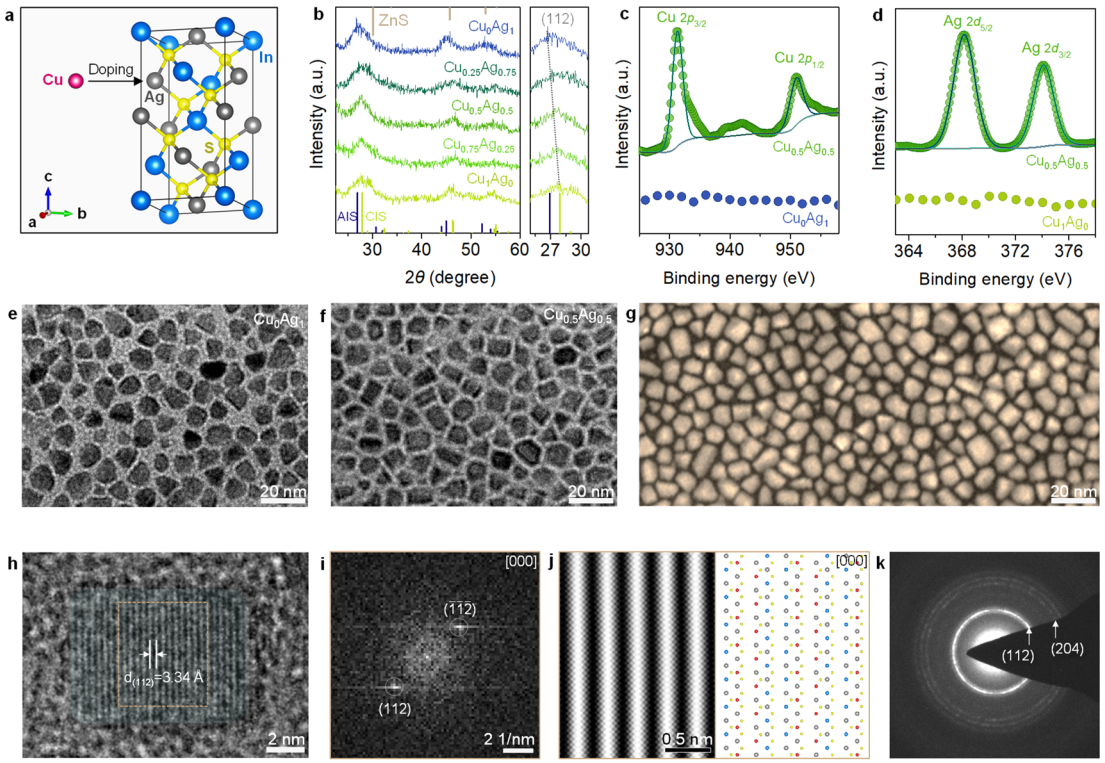

Figure 2. Structural characterization of $Cu_xAg_{1-x}InS_2$/ZnS CQDs: (a) Schematic presentation of $AgInS_2$ chalcopyrite structure. (b) XRD patterns of $Cu_xAg_{1-x}InS_2$/ZnS CQDs (x = 0, 0.25, 0.5, 0.75, and 1). The zoomed-in image on the right side shows the $AgInS_2$ (112) and $CuInS_2$ (112) diffraction peaks. Binding energy of (c) Cu 2p and (d) Ag 2d in $Cu_xAg_{1-x}InS_2$/ZnS CQDs (x = 0, 0.5, and 1). TEM images of (e) Cu_0Ag_1 CQDs and (f) $Cu_{0.5}Ag_{0.5}$ CQDs. (g) STEM image, (h) HRTEM image, and (k) selected-area electron diffraction pattern of $Cu_{0.5}Ag_{0.5}$ CQDs. (i) Calculated FFTs of HRTEM images from the yellow boxed region in (h). (j) Lattice averaged image from the yellow area in (h) reveals the atomic arrangement along the [000] direction. The atomic arrangement fits well with the chalcopyrite $AgInS_2$ crystal structure. Here and in (j), colors represent the following: red, copper; gray, silver; blue, indium; yellow, sulfur.

2. RESULTS AND DISCUSSION

The $AgInS_2$ and $AgInS_2$/ZnS CQDs (Figure 1e) were synthesized at different reaction temperatures, showing the tunable photoluminescence emission colors (Figure S1b and Figure S1c). After ZnS shell growth, $AgInS_2$/ZnS CQDs exhibit longer photoluminescence lifetimes compared with that of $AgInS_2$ CQDs (Figure 1f and Table S1). This indicates that ZnS shell-assisted surface passivation can reduce the defect-state concentration and eliminate some surface-related non-radiative centers, which are beneficial for photocatalytic applications.[34] Among all $AgInS_2$-based CQDs, $AgInS_2$/ZnS CQDs synthesized at 180 °C show the best photoactivity (Figure S1d), and hence $AgInS_2$/ZnS CQDs (180 °C) were chosen as the model catalyst for study in this work. More details of the CQD synthesis can be seen in the Experimental Section of the Supporting Information.

The core/shell $Cu_xAg_{1-x}InS_2$/ZnS CQDs with different Cu/Ag molar ratios (x = 0, 0.25, 0.5, 0.75, and 1) were synthesized at 180 °C by a hot-injection method. The Cu-to-Ag atomic ratio was supported by an inductively coupled plasma−optical emission measurement (Table S2). For clarity, the $AgInS_2$/ZnS, $Cu_{0.25}Ag_{0.75}InS_2$/ZnS, $Cu_{0.5}Ag_{0.5}InS_2$/ZnS, $Cu_{0.75}Ag_{0.25}InS_2$/ZnS, and $CuInS_2$/ZnS are denoted as Cu_0Ag_1, $Cu_{0.25}Ag_{0.75}$, $Cu_{0.5}Ag_{0.5}$, $Cu_{0.75}Ag_{0.25}$, and Cu_1Ag_0 hereafter, respectively. The tunable dopant Cu(I) ions are doped into the $AgInS_2$ structure during the growth of host core CQDs with Cu atoms instead of Ag atoms (Figure 2a). As shown in Figure 2b, all $Cu_xAg_{1-x}InS_2$/ZnS samples exhibit the diffraction peaks of X-ray diffraction (XRD), consistent with a tetragonal structure of $AgInS_2$ (AIS, see JCPDS database file 25-1330)[35] and $CuInS_2$ (CIS, see JCPDS database file 47-1372),[36] implying the crystal structure was not changed after doping Cu into the $Cu_xAg_{1-x}InS_2$/ZnS CQDs (Figure S1a). Moreover, carefully calibrated XRD spectra (right image of Figure 2b) suggest the increasing Cu concentration makes a red-shift of the diffraction peaks to larger angles. This is because the ionic radius of Cu (74 pm) is smaller than that of Ag (114 pm), leading to a lattice contraction after the Cu doping. Furthermore, the chemical compositions of $Cu_xAg_{1-x}InS_2$/ZnS-alloyed CQDs were investigated by X-ray photoelectron spectroscopy (XPS). Figure 2c displays high-resolution scans of Cu 2p, showing two major fitting peaks at 930.6 and 951.3 eV corresponding to Cu $2p_{3/2}$ and Cu $2p_{1/2}$ for Cu^+, respectively. In Figure 2d, the binding energies at 367.6 and 373.7 eV are assigned to Ag $3d_{5/2}$ and Ag $3d_{3/2}$ for Ag^+ ions, respectively. In addition, the typical In 3d, Zn 2p, and S 2p level spectra are shown in Figure S2, indicating that the normal valence states for $Cu_xAg_{1-x}InS_2$/ZnS are $3d_{5/2}$ $3d_{3/2}$ for In, $2p_{3/2}$ $2p_{1/2}$ for S, and $2p_{3/2}$ $2p_{1/2}$ for Zn.[37]

The $Cu_xAg_{1-x}InS_2$/ZnS-alloyed CQDs were further characterized by transmission electron microscopy (TEM). In Figure 2e and 2f, the average dimeter of the as-prepared Cu_0Ag_1 and $Cu_{0.5}Ag_{0.5}$ CQDs was about 8.6 and 8.8 nm, respectively (Figure S3), suggesting the nanoparticle size remained almost constant with the variation of the Cu doping ratio. Furthermore, scanning transmission electron microscopy (STEM) analysis confirms the uniform size distribution of $Cu_{0.5}Ag_{0.5}$ CQDs (Figure 2g). The high-resolution trans-

https://doi.org/10.1021/acsomega.1c07045
ACS Omega 2022, 7, 9642−9651

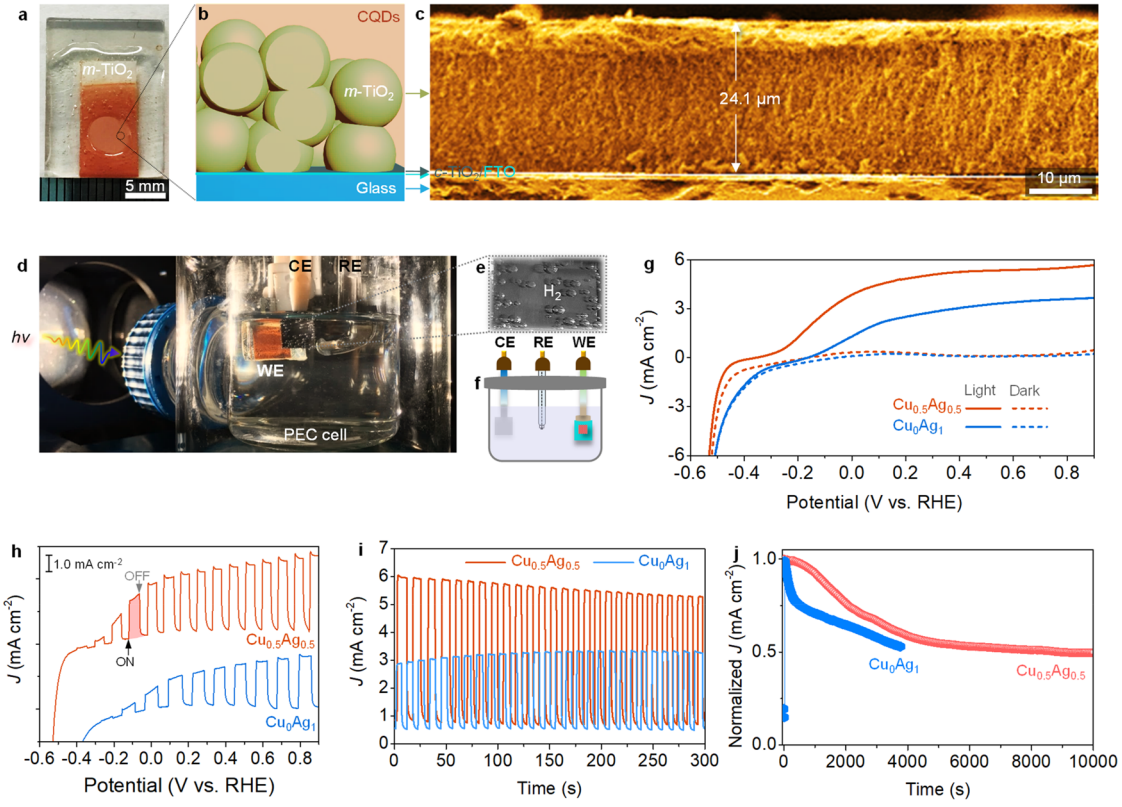

Figure 3. PEC properties of $Cu_xAg_{1-x}InS_2$/ZnS CQD-sensitized TiO_2 photoanodes: (a) photograph, (b) illustrative schematic, and (c) cross-sectional SEM image of the glass|FTO|TiO_2|CQD-sensitized photoanode. (d) Photograph and (f) scheme of CQD-sensitized PEC cells. (e) Photograph of the Pt counter electrode. (g) Photocurrent measurement with linear sweep voltammetry for CQD-sensitized PEC cells in the dark and under AM 1.5 G illumination at 100 mW cm^{-2}. (h) Photocurrent density−bias potential dependence and (i) photocurrent density−time dependence (at 0.5 V) of CQD-sensitized PEC cells in the chopped AM 1.5G irradiation. (j) Normalized steady-state photocurrent density as a function of time of CQD-sensitized PEC cells at 0.5 V (vs RHE) under AM 1.5 G illumination at 100 mW cm^{-2}.

mission electron microscopy (HR-TEM) images further show that the $Cu_{0.5}Ag_{0.5}$ CQDs were largely single crystalline in nature, as shown in Figure 2h. The interplanar distance of 3.34 Å corresponds to the (112) plane for typical chalcopyrite $AgInS_2$. The $Cu_{0.5}Ag_{0.5}$ CQDs were imaged with one crystallographic direction, viz., [000], indicated by the yellow area. When fast Fourier transformation (FFT) is calculated from the area, the characteristic lattice of chalcopyrite $AgInS_2$ is directly evident in Figure 2i. The clear atomic arrangement fits well with the $AgInS_2$ crystal structure in the direction, as can be seen in the models depicted in Figure 2j, confirming the chalcopyrite crystal structure of the $Cu_{0.5}Ag_{0.5}$ CQDs. In addition, electron diffraction circles from the (112) and (204) crystallographic planes were observed in Figure 2k, showing the intensity profile of the diffraction rings corresponding to the XRD data.

To investigate the potential of these Cu-doped CQDs for PEC H_2 production, the $Cu_xAg_{1-x}InS_2$/ZnS CQD-sensitized TiO_2 photoanodes (Figure 3a) were prepared by depositing CQDs into the mesoporous TiO_2 (m-TiO_2) film substrates by the EPD method (detailed information in the Supporting Information).[38] The schematic diagram of glass|FTO|TiO_2|$Cu_xAg_{1-x}InS_2$/ZnS CQD-sensitized photoanodes is displayed in Figure 3b. The corresponding $Cu_{0.5}Ag_{0.5}$ CQD-sensitized TiO_2 photoanode has a 24.1 μm thickness of the m-TiO_2 layer (Figure 3c). The PEC performance of the $Cu_xAg_{1-x}InS_2$/ZnS CQD-sensitized photoanodes was measured in the dark and under simulated solar illumination (AM 1.5 G, 100 mW cm^{-2}). The measurements were performed using the architecture of a standard three-electrode configuration with a working electrode (as-fabricated CQD-sensitized photoanode), Pt counter electrode, and Ag/AgCl reference electrode (Figure 3d and 3f). As shown in Figure 3g and Figure S4, the photocurrent density (J) of the Cu_0Ag_1 and Cu_1Ag_0 CQD photoanodes is about 3.6 and 3.4 mA cm^{-2} at 0.9 V_{RHE} (reversible hydrogen electrode; detailed information in the Supporting Information), respectively, while the bare TiO_2 photoanode shows a very low saturated J = 0.38 mA cm^{-2} (Figure S5). The results confirm that high hydrogen production activity with the enhanced photocurrent density is mainly ascribed to the CQD photoelectrocatalysts deposited on the TiO_2 film. For comparison, the saturated photocurrent density of the $Cu_{0.5}Ag_{0.5}$ CQD photoanode-based PEC is improved to 5.8 mA cm^{-2}, showing the 1.7 times enhancement compared to that of pristine CQDs because of the Cu doping. In addition, the corresponding calculated H_2 generation rate (see Figure S6 in the Supporting Information) is up to 67.4 μmol cm^{-2} h^{-1} for $Cu_{0.5}Ag_{0.5}$ CQDs from 36.4 μmol cm^{-2} h^{-1} for Cu_0Ag_1 CQDs, which is obtained by using the measured photocurrent as a reference.[39] These results demonstrate that Cu doping in AIS CQDs can effectively improve the H_2 generation performance of the CQD-sensitized system.

Meanwhile, Figure 3h shows the photocurrent density versus the applied bias (vs RHE) for the Cu_0Ag_1 and $Cu_{0.5}Ag_{0.5}$ CQD PEC cells in the S^{2-}/SO_3^{2-}electrolyte during the on−off illumination cycles. Significantly, a spike in the photocurrent

https://doi.org/10.1021/acsomega.1c07045
ACS Omega 2022, 7, 9642−9651

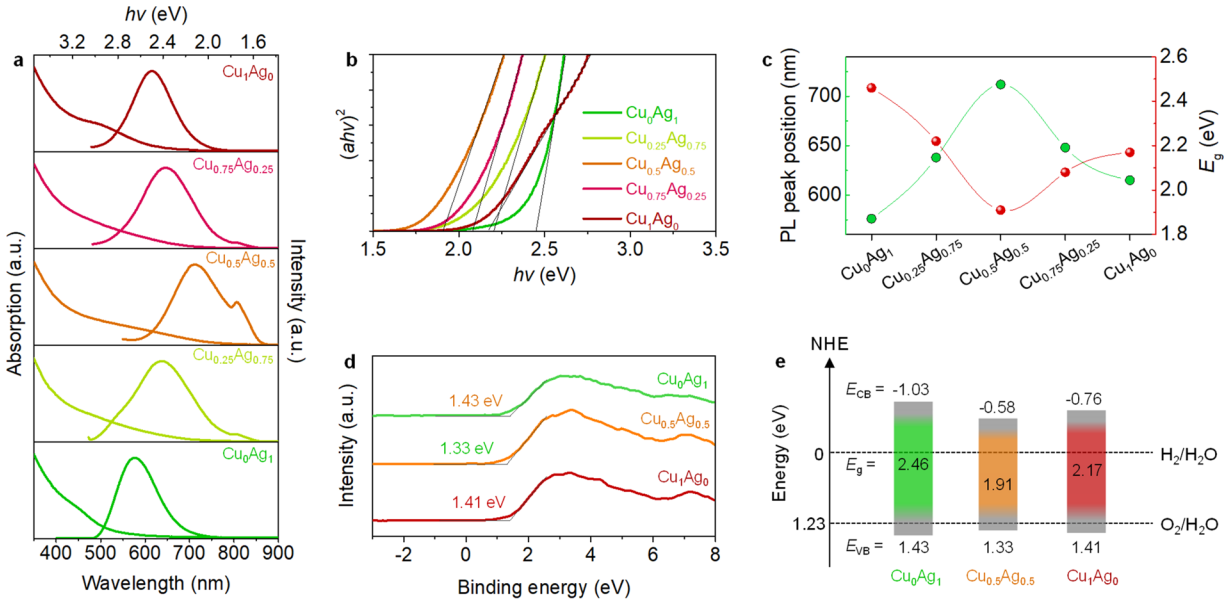

Figure 4. Optical properties and band structure of $Cu_xAg_{1-x}InS_2$/ZnS CQDs: (a) UV−vis absorption spectra and photoluminescence (PL) spectra and (b) Tauc plots of UV−vis absorption spectra for $Cu_xAg_{1-x}InS_2$/ZnS CQDs (x = 0, 0.25, 0.5, 0.75, and 1). The black lines represent the extrapolation of the linear portion of the absorption edges, α, absorption coefficient; h, Planck's constant; and ν, photon frequency. (c) PL peak position and E_g versus Cu doping content. (d) Valence band (VB) XPS spectra and (e) the corresponding energy band diagram for $Cu_xAg_{1-x}InS_2$/ZnS CQDs (x = 0, 0.5, and 1).

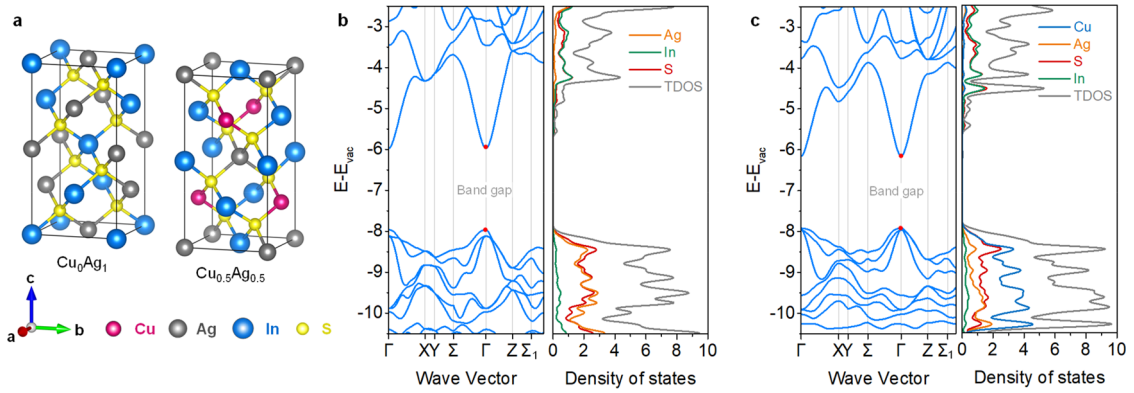

Figure 5. DFT calculations: (a) Atomic structures of Cu_0Ag_1 and $Cu_{0.5}Ag_{0.5}$ used in DFT calculations. The energy band structure and density of states (DOS) of (b) Cu_0Ag_1 and (c) $Cu_{0.5}Ag_{0.5}$ calculated with the PBE0 level, where the energy level was aligned with respect to the vacuum level (E_{vac}).

density of $Cu_{0.5}Ag_{0.5}$ CQDs is more obvious tha that of pristine CQDs in Figure 3h and Figure S4. It is mainly attributed to good charge separation and fast charge transport due to the introduction of Cu doping. Furthermore, the photocurrent density versus reaction time of CQDs based on PEC cells at 0.5 V_{RHE} upon standard on/off irradiation is displayed in Figure 3i. It can be seen that the obvious enhancement in photocurrent density of the $Cu_{0.5}Ag_{0.5}$ CQD PEC cell is obtained compared to that of the Cu_0Ag_1 CQDs. Higher photocurrent density indicates that more photogenerated electrons can be transferred to the counter electrode derived from the CQD photoanode. The stability measurements of the PEC cell based on $Cu_xAg_{1-x}InS_2$/ZnS CQD photoanodes were investigated at 0.5 V versus RHE under AM 1.5 G solar illumination (100 mW cm^{-2}). In Figure 3j, the photocurrent density of Cu_0Ag_1 CQD-based PEC cells rapidly decreases during illumination, showing a large degradation (≈52%) of its initial value after 4000 s. However, 60% of the initial value for the $Cu_{0.5}Ag_{0.5}$ CQD photoanodes can be maintained after 4000 s solar illumination, and a drop equals to 50% after 10 000 s, exhibiting the improvement in chemical- and photostability in this $Cu_xAg_{1-x}InS_2$/ZnS CQD-sensitized photoanode for PEC cells due to Cu doping.

To investigate the photophysical origins of the enhanced photoelectrocatalytic performance with different Cu doping concentrations, the optical properties of the $Cu_xAg_{1-x}InS_2$/ZnS CQD contents were studied. In Figure 4a, PL peak position first red-shifted and subsequently blue-shifted with a peak at 750 nm as the Cu doping content increases. It is in accord with the trend of an absorption edge shift with or without a ZnS shell (Figure S7). The corresponding spectral data are displayed in the Supporting Information Table S3. The optical bandgaps (E_g) of Cu_0Ag_1, $Cu_{0.25}Ag_{0.75}$, $Cu_{0.5}Ag_{0.5}$, $Cu_{0.75}Ag_{0.25}$, and Cu_1Ag_0 are calculated to be 2.46, 2.22, 1.91, 2.08, and 2.17 eV, respectively, according to the classical Tauc method (Figure 4b). It finds that the E_g first augments and

https://doi.org/10.1021/acsomega.1c07045
ACS Omega 2022, 7, 9642−9651

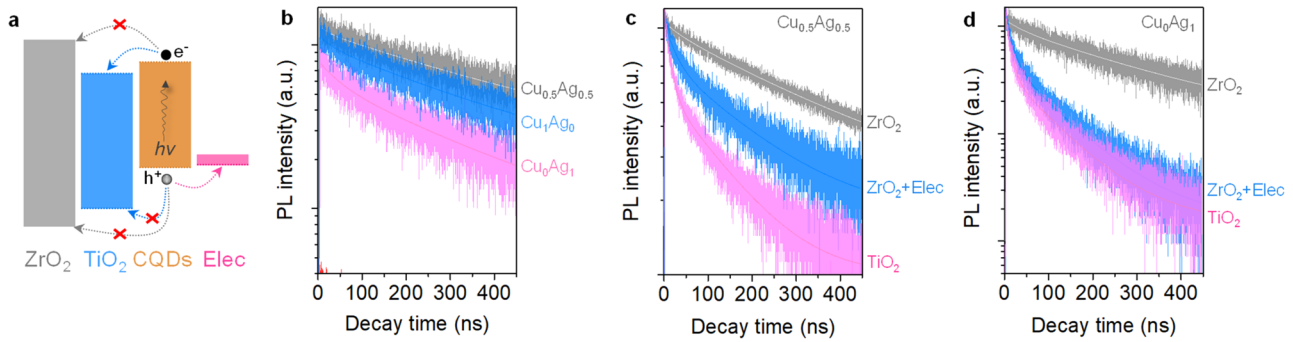

Figure 6. Photoluminescence properties of $Cu_xAg_{1-x}InS_2$/ZnS CQDs: (a) Schematic diagram of the energy gap structure of ZrO_2/TiO_2/CQD/Elec, showing the charge-transfer process. (b) Photoluminescence decay curves of $Cu_xAg_{1-x}InS_2$/ZnS CQDs (x = 0, 0.5, and 1). Photoluminescence decay curves of (c) $Cu_{0.5}Ag_{0.5}$ and (d) Cu_0Ag_1 CQDs on TiO_2, ZrO_2, and ZrO_2 wetted with the electrolyte (ZrO_2 + Elec).

subsequently decreases with a minimum value of 1.91 eV for $Cu_{0.5}Ag_{0.5}$ CQDs (Figure 4c). The observation reveals that the Cu ions are successfully doped into the $AgInS_2$ CQDs to produce light absorption and PL emission and change the lattice energy band. This result provides evidence and support to previous reports of the extent of the Cu-to-Ag ratio in the optical property alteration by the lattice structure compatibility theory.[40] It also confirms the potential of Cu doping engineering to enhance the optical property and optimize the band structure of the $AgInS_2$ CQDs.

To further characterize the electronic states and band structures of $Cu_xAg_{1-x}InS_2$/ZnS CQDs with different Cu doping concentrations, the valence band positions of Cu_0Ag_1, $Cu_{0.5}Ag_{0.5}$, and Cu_1Ag_0 were measured by the secondary electron cutoff and valence band spectra from He I excitation energy (Figure 4d), which are calculated to be 1.43, 1.33, and 1.41 eV, respectively. Based on the measured band energies, the band alignment diagram of Cu_0Ag_1, $Cu_{0.5}Ag_{0.5}$, and Cu_1Ag_0 CQDs is shown in Figure 4e, demonstrating that the conduction band (E_{CB}) potentials vs NHE are calculated as −1.03, −0.58, and −0.76 eV, respectively. Compared to the pristine AIS or CIS CQDs, both the conduction band (CB) and valence band (VB) of the Cu-doped CQD are found to shift negatively. This finding further confirms that the band structure can been designed by tailoring the Cu dopant concentration, narrowing the bandgap and leading to an obvious enhancement of visible-light absorption. This also demonstrates that the tunable band structure is expected to increase the charge transfer efficiency by drift of the photogenerated electrons to the CQDs/TiO_2 interface and of the photogenerated holes to the CQDs/electrolyte interface.[41]

Thus, we further investigated the effect of Cu doping in the $AgInS_2$ atomic electronic structure by density functional theory (DFT) calculations. Figure 5a shows the pristine atomic structure of Cu_0Ag_1 with space group I-42d (122) with the chalcopyrite lattice. The unit cell contains 4 Ag, 4 In, and 8 S atoms, containing the AgS_4 and InS_4 tetrahedra. In Figure 5b, the doped structure of Cu_0Ag_1 has a direct band gap energy of 1.99 eV. After Cu doping, the calculated band gap energy of $Cu_{0.5}Ag_{0.5}$ is decreased to 1.77 eV, which is close to the experimental value. Moreover, the calculated total density of states (TDOS) spectra show that the valence band maximum (VBM) of Cu_0Ag_1 consists of the Ag and S atom hybrid orbitals, and the conduction band minimum (CBM) is mainly attributed to the In and S atom hybrid orbitals. It is obvious that Cu doping shifts the VBM of $Cu_{0.5}Ag_{0.5}$ upward and narrows the band gap because of the participation of the Cu atom orbitals (Figure 5c). It could be the reason that the d orbital of the Cu atoms possesses slightly higher energy than that of the Ag d orbital.[42] Therefore, the Cu doping can tailor both the band gap energy and band edge position of AIS CQDs. These results suggest that the Cu doping effect is able to create the efficient transportation and separation of the photogenerated charge for CQDs/TiO_2 heterojunction photoanodes for photocatalytic hydrogen generation in the PEC cell.[43]

To gain insight into the separation efficiency of photogenerated electrons and holes, time-resolved photoluminescence (PL) spectra of Cu_0Ag_1, $Cu_{0.5}Ag_{0.5}$, and Cu_1Ag_0 CQDs were displayed in Figure 6b under 350 nm excitation, and the corresponding data were fitted by a biexponential model[44] (see eqs S1−S2 in the Supporting Information). Compared to pure CQDs, the PL decay time of the $Cu_{0.5}Ag_{0.5}$ CQDs increases upon doping with Cu content of 50% (Table S1), now having a prolonged lifetime of 397.9 ns. This extension of carrier lifetimes demonstrates the effective spatial separation of charge carriers, which are beneficial for photoelectrocatalytic application in the CQD system.[45] In fact, the longer lifetime is attributed to the exciton relaxation derived from the host CQD systems via the additional Cu T_2 energy states.[27,29]

To further investigate the electron transfer rate (K_{et}) and hole transfer rate (K_{ht}), the transient PL spectra of $Cu_xAg_{1-x}InS_2$/ZnS CQDs deposited on TiO_2 or ZrO_2 films with or without dipping the S^{2-}/SO_3^{2-} electrolyte are shown in Figure 6c,d. The K_{et} or K_{ht} is calculated by using the following eq 1[43,46,47]

$$k_{\text{et or ht}} = \frac{1}{\tau_{\text{QDs/(TiO}_2\text{ or ZrO}_2\text{/Elec)}}} - \frac{1}{\tau_{\text{QDs/ZrO}_2}} \quad (1)$$

where $\tau_{QDs/TiO2}$ and $\tau_{QDs/ZrO2}$ are the PL lifetime of $Cu_xAg_{1-x}InS_2$/ZnS CQDs deposited on TiO_2 and ZrO_2 substrates, respectively, indicating the efficiency of the photogenerated carrier separation and transport,[48] and $\tau_{QDs/ZrO2/Elec}$ represents the PL lifetime of CQDs deposited on ZrO_2 with the presence of the electrolyte (Figure 6a). The carrier transfer rates are reported in Table S4. Generally, the electrons or holes transfer from CQDs to TiO_2 or ZrO_2 with a hole scavenger with a suitable energy level. The K_{et} value is 1.9 times larger than K_{ht}, suggesting a more efficient electron transfer from $Cu_{0.5}Ag_{0.5}$ CQDs toward that of TiO_2, compared to that of Cu_0Ag_1 CQDs (1.2 times). These results indicate that an efficient photoexcited electron and hole transfer can be

https://doi.org/10.1021/acsomega.1c07045
ACS Omega 2022, 7, 9642−9651

achieved by controlling the Cu doping, confirming the enhanced performance of Cu-doping CQDs in the PEC solar H_2 generation.

3. CONCLUSIONS

In summary, heavy metal-free $Cu_xAg_{1-x}InS_2$/ZnS CQDs with different Cu doping profiles were prepared by in situ growth with a hot-injection method. The effects of Cu doping on light absorption and band energetics of $AgInS_2$ CQDs were studied with a ZnS shell-assisted defect passivation strategy. It is found that the Cu doping obviously shifts the band edge positions of $AgInS_2$ CQDs and optimizes the optical properties. The Cu doping improves the efficiency of the photogenerated charge separation by tailoring a suitable energy band structure. Based on these findings, the $Cu_{0.5}Ag_{0.5}InS_2$/ZnS CQD-sensitized TiO_2 photoanode for the PEC cell shows an excellent photocurrent density of 5.8 mA cm^{-2}. In addition, the doping effects and shell defect passivation also lead to an improvement in stability with 50% surplus of the photocurrent density for 10 000 s. These results demonstrate that the use of this designed Cu doping strategy with defect passivation can be used as a guideline for improving the photoelectrocatalytic activities of heavy metal-free I−III−VI CQD light absorbers for PEC hydrogen generation.

4. EXPERIMENTAL SECTION

4.1. Materials. Copper iodide (CuI, 99.999%), silver nitrate ($AgNO_3$, 99.99%), indium acetate ($In(Ac)_3$, 99.99%), sulfur (S, 99%), zinc acetate dehydrate ($Zn(Ac)_2{\cdot}2H_2O$), 1-octadecence (ODE, 99.6%), 1-dodecanethiol (DDT, 96%), trioctylphospine (TOP, 90%), oleylamine (OLA, 70%), sodium sulfite (Na_2SO_3), sodium sulfide nonahydrate ($Na_2S{\cdot}9H_2O$), acetone (>99%), methanol (99.93%), and ZrO_2 nanoparticle powder (≈100 nm sized) were bought from Sigma. Ti-nanoxide was purchased from Solaronix. Titania (TiO_2) paste (18 NR-AO, 20−450 nm sized) was obtained from Dyesol (Queanbeyan, Australia). The FTO/glass substrates were bought from XOP Glass Co., Ltd. All chemicals were used without further purification.

4.2. Synthesis of $Cu_xAg_{1-x}InS_2$/ZnS CQDs. The synthesis of $Cu_xAg_{1-x}InS_2$/ZnS CQDs with tunable molar ratio of Ag/Cu followed the reference with slight modifications.[34] The $Cu_xAg_{1-x}InS_2$/ZnS CQD was synthesized via a hot-injected method using different Ag and Cu precursors. Typically, 0.051 g of $AgNO_3$ and 0.09 g of $In(Ac)_3$ were mixed with 24 mL of ODE in a flask and then purged by N_2 gas for 30 min. Subsequently, the temperature was raised to 100 °C. Then 3 mL of DDT was added in the flask and heated to different reaction temperature (130, 180, and 210 °C, respectively). Then, 0.02 g of S and 1.3 mL of OLA mixed solution were quickly injected into the flask with vigorous stirring for 30 min. For ZnS shell *in situ* growth, 0.762 g of $Zn(Ac)_2$, 0.0384 g of S, and 6 mL of TOP mixed clear solution were quickly injected into the above reaction solution and then kept at the corresponding temperature for 2 h. After the reaction finished, the anhydrous ethanol was added into the reaction solution, and the obtained suspension was centrifuged. Finally, the as-synthesized $Cu_xAg_{1-x}InS_2$/ZnS CQDs were dispersed in toluene. The additive amount of CuI is the 0, 25, 50, 75, and 100% the molar weight of $AgNO_3$, respectively. The same process was used to synthesis a series of the $Cu_xAg_{1-x}InS_2$/ZnS CQDs.

4.3. Preparation of TiO_2 and ZrO_2 Films. The compact TiO_2 layers were deposited on clear FTO/glass substrates by spinning TiO_2 precursor solution (Ti-Nanoxide) at 5000 r.p.m. for 30 s and then sintered at 500 °C for 30 min. Subsequently, the mesoporous TiO_2 layers were deposited on the above-mentioned substrates by blade-coating 18 NR-AO TiO_2 paste. Finally, the films were sintered at 500 °C for 30 min. For the mesoporous ZrO_2 films, the same blade-coating process and thermal treatment procedure were performed by using the commercial ZrO_2 paste.

4.4. Fabrication of CQD-Based Photoelectrochemical Cells. The CQD-based photoelectrochemical (PEC) cells were constructed by a typical three-electrode configuration, consisting of a CQD-TiO_2 electrode, a Pt counter electrode, a saturated Ag/AgCl reference electrode, and the electrolyte. The $Cu_xAg_{1-x}InS_2$ and $Cu_xAg_{1-x}InS_2$/ZnS CQDs were deposited on a TiO_2/FTO/glass substrate with a current bias of 100 V for 2 h in CQD toluene solution according to the electrophoretic deposition method.[49] Subsequently, the surface of the as-prepared CQDs-TiO_2 electrodes was protected by depositing a ZnS capping layer via the SILAR deposition cycle[47] to complete PEC cell fabrication. The active area of the photoanode ranges is 0.15 ± 0.05 cm^2.

4.5. Characterization. X-ray diffraction of the CQD samples was carried out with a Philips X'Pert PRO X-ray diffractometer. X-ray photoelectron spectroscopy measurement was performed on a VG Escalab 220i-XL electron spectrometer by using a Twin Anode X-ray Source. Inductively coupled plasma-optical emission measurements were carried out with an Agilent 5100 ICP-OES system. Transmission electron microscopy images of the CQD samples were recorded using a JEOL ARM200CF TEM/STEM at an accelerating voltage of 200 kV. UV−vis spectra were performed on a Shimadzu UV-2600 spectrophotometer. Steady-state photoluminescence measurements were performed by using the Horiba Jobin Yvon. Time-resolved photoluminescence measurements were taken by a Pico-Quant FmbH fluorescence lifetime spectrometer. The morphology images of cross-sectional CQD-TiO_2 electrodes were obtained with a JSM-7401F scanning electron microscope. Current−potential measurements of the CQD-based photoelectrochemical cells were performed in a potential window of −0.6 V to +0.9 V versus the reversible hydrogen electrode (RHE) ($V_{RHE} = V_{Ag/AgCl} + 0.1976 + 0.059 \times pH$) by using simulated one-sun illumination (AM 1.5G, 100 mW cm^{-2}) with a SLB-300A solar simulator with a CHI-760D electrochemical workstation.

4.6. Theoretical Method. Structure optimization and electronic structure calculations were recorded by using density functional theory (DFT) with the projector-augmented wave (PAW) method,[50] as implemented in the Vienna Ab initio Simulation Package (VASP).[51,52] A cutoff energy of 500 eV and an 8 × 8 × 8 Monkhorst−Pack k-point mesh were used in all calculations. All structures are fully optimized with the maximum atomic force below 0.01 eV $Å^{-1}$, and the convergence criterion of electronic energy was set to 10^{-5} eV. The Perdew−Burke−Ernzerhof (PBE)[53] and hybrid PBE0[54] exchange-correlation functional were used for structure optimization and electronic structure calculation, respectively. Band structures within the hybrid functional scheme were obtained for efficiency by using the smoothed Fourier interpolation which was implemented in the BoltzTraP2 code.[55] For band alignment, the energy levels, including the valence band maximum (VBM), conduction band minimum

https://doi.org/10.1021/acsomega.1c07045
ACS Omega 2022, 7, 9642−9651

(CBM), and Fermi level, are referenced to the vacuum level. To obtain the vacuum level of the bulk system, the slab models with a vacuum layer of 20 Å were constructed using the 1 × 1 × 5 supercell of conventional cells. Then the value of the energy level with respect to the vacuum level can be defined uniformly as $E = (E^{bulk} - E^{bulk}_{ref}) - (E^{slab}_{vac} - E^{slab,far}_{ref})$, where E^{bulk} is the energy level of the bulk system; E^{slab}_{vac} is the vacuum level of the slab system; and E^{bulk}_{ref} and $E^{slab,far}_{ref}$ are the macroscopically averaged electrostatic potential in the bulk system and the region far away from the surface of the slab system, respectively.

■ ASSOCIATED CONTENT

Supporting Information

The Supporting Information is available free of charge at https://pubs.acs.org/doi/10.1021/acsomega.1c07045.

XRD patterns, UV−vis absorption spectra, PL spectra, photocurrent measurement with linear sweep voltammetry (Figure S1); XPS spectra (Figure S2); size distributions (Figure S3); photocurrent measurement of pristine CQDs (Figure S4); photocurrent measurement of TiO_2 (Figure S5); H_2 evolution rate (Figure S6); UV−vis absorption spectra (Figure S7); fitted parameters of TRPL (Table S1); ICP data (Table S2); optical data (Table S3); and electron and hole transfer rate (Table S4) (PDF)

■ AUTHOR INFORMATION

Corresponding Authors

Heng Guo − *School of New Energy and Materials, Institute of Carbon Neutrality, Southwest Petroleum University, Chengdu 610500, China*; orcid.org/0000-0002-8117-6790; Email: heng.guo@swpu.edu.cn

Haiyuan Chen − *School of Materials and Energy, University of Electronic Science and Technology of China, Chengdu 610054, China*; Email: hychen@uestc.edu.cn

Authors

Peng Yang − *School of New Energy and Materials, Institute of Carbon Neutrality, Southwest Petroleum University, Chengdu 610500, China*

Jie Hu − *School of Materials and Energy, University of Electronic Science and Technology of China, Chengdu 610054, China*

Anqiang Jiang − *School of New Energy and Materials, Institute of Carbon Neutrality, Southwest Petroleum University, Chengdu 610500, China*

Xiaobin Niu − *School of Materials and Energy, University of Electronic Science and Technology of China, Chengdu 610054, China*

Ying Zhou − *School of New Energy and Materials, Institute of Carbon Neutrality, Southwest Petroleum University, Chengdu 610500, China*; orcid.org/0000-0001-9995-0652

Complete contact information is available at: https://pubs.acs.org/10.1021/acsomega.1c07045

Author Contributions

The paper was completed by contributions of all the authors. All the authors approved the final version of the paper.

Notes

The authors declare no competing financial interest.

■ ACKNOWLEDGMENTS

This work was supported by the National Key R&D Program of China (2020YFA0710000), the National Natural Science Foundation of China (Grant No.: 22109132, 11904047, 22178291, 11974004, and 22002123), the Provincial Key Research and Development Project of Sichuan (2021YFSY0046), the Scientific Research Starting Project of SWPU (2019QHZ010), Science and Technology Innovation Fund for College Students of SWPU (No. 2020KSP05044), and the China Postdoctoral Science Foundation (2019M663460).

■ REFERENCES

(1) Navarro-Pardo, F.; Zhao, H.; Wang, Z. M.; Rosei, F. Structure/Property Relations in "Giant" Semiconductor Nanocrystals: Opportunities in Photonics and Electronics. *Acc. Chem. Res.* **2018**, *51*, 609−618.

(2) Zhao, H.; Rosei, F. Colloidal Quantum Dots for Solar Technologies. *Chem.* **2017**, *3*, 229−258.

(3) Coughlan, C.; Ibanez, M.; Dobrozhan, O.; Singh, A.; Cabot, A.; Ryan, K. M. Compound Copper Chalcogenide Nanocrystals. *Chem. Rev.* **2017**, *117*, 5865−6109.

(4) Choi, M.-J.; Kim, Y.; Lim, H.; Alarousu, E.; Adhikari, A.; Shaheen, B. S.; Kim, Y. H.; Mohammed, O. F.; Sargent, E. H.; Kim, J. Y.; Jung, Y. S. Tuning Solute-Redistribution Dynamics for Scalable Fabrication of Colloidal Quantum-Dot Optoelectronics. *Adv. Mater.* **2019**, *31*, 1805886.

(5) Kagan, C. R.; Lifshitz, E.; Sargent, E. H.; Talapin, D. V. Building Devices from Colloidal Quantum Dots. *Science* **2016**, *353*, aac5523.

(6) Swarnkar, A.; Marshall, A. R.; Sanehira, E. M.; Chernomordik, B. D.; Moore, D. T.; Christians, J. A.; Chakrabarti, T.; Luther, J. M. Quantum Dot-Induced Phase Stabilization of α-$CsPbI_3$ Perovskite for High-Efficiency Photovoltaics. *Science* **2016**, *354*, 92−95.

(7) Sanehira, E. M.; Marshall, A. R.; Christians, J. A.; Harvey, S. P.; Ciesielski, P. N.; Wheeler, L. M.; Schulz, P.; Lin, L. Y.; Beard, M. C.; Luther, J. M. Enhanced Mobility $CsPbI_3$ Quantum Dot Arrays for Record-Efficiency, High-Voltage Photovoltaic Cells. *Sci. Adv.* **2017**, *3*, eaao4204.

(8) Song, J.; Xu, L.; Li, J.; Xue, J.; Dong, Y.; Li, X.; Zeng, H. Monolayer and Few-Layer All-Inorganic Perovskites as a New Family of Two-Dimensional Semiconductors for Printable Optoelectronic Devices. *Adv. Mater.* **2016**, *28*, 4861−4869.

(9) Li, X.; Tong, X.; Yue, S.; Liu, C.; Channa, A. I.; You, Y.; Wang, R.; Long, Z.; Zhang, Z.; Zhao, Z.; Liu, X. F.; Wang, Z. M. Rational Design of Colloidal $AgGaS_2$/CdSe Core/Shell Quantum Dots for Solar Energy Conversion and Light Detection. *Nano Energy* **2021**, *89*, 106392.

(10) Pan, J.; Shang, Y.; Yin, J.; De Bastiani, M.; Peng, W.; Dursun, I.; Sinatra, L.; El-Zohry, A. M.; Hedhili, M. N.; Emwas, A. H.; Mohammed, O. F.; Ning, Z.; Bakr, O. M. Bidentate Ligand-Passivated $CsPbI_3$ Perovskite Nanocrystals for Stable near-Unity Photoluminescence Quantum Yield and Efficient Red Light-Emitting Diodes. *J. Am. Chem. Soc.* **2018**, *140*, 562−565.

(11) Dai, X.; Zhang, Z.; Jin, Y.; Niu, Y.; Cao, H.; Liang, X.; Chen, L.; Wang, J.; Peng, X. Solution-Processed, High-Performance Light-Emitting Diodes Based on Quantum Dots. *Nature* **2014**, *515*, 96−99.

(12) Gong, X.; Yang, Z.; Walters, G.; Comin, R.; Ning, Z.; Beauregard, E.; Adinolfi, V.; Voznyy, O.; Sargent, E. H. Highly Efficient Quantum Dot near-Infrared Light-Emitting Diodes. *Nat. Photonics* **2016**, *10*, 253−257.

(13) Won, Y.-H.; Cho, O.; Kim, T.; Chung, D.-Y.; Kim, T.; Chung, H.; Jang, H.; Lee, J.; Kim, D.; Jang, E. Highly Efficient and Stable InP/ZnSe/ZnS Quantum Dot Light-Emitting Diodes. *Nature* **2019**, *575*, 634−638.

(14) Yan, Y.; Crisp, R. W.; Gu, J.; Chernomordik, B. D.; Pach, G. F.; Marshall, A.; Turner, J. A.; Beard, M. C. Multiple Exciton Generation

for Photoelectrochemical Hydrogen Evolution Reactions with Quantum Yields Exceeding 100%. *Nat. Energy* **2017**, *2*, 17052.
(15) Smith, A. M.; Nie, S. Semiconductor Nanocrystals: Structure, Properties, and Band Gap Engineering. *Acc. Chem. Res.* **2010**, *43*, 190−200.
(16) Gratzel, M. Photoelectrochemical Cells. *Nature* **2001**, *414*, 338−344.
(17) Tong, X.; Kong, X. T.; Wang, C.; Zhou, Y.; Navarro-Pardo, F.; Barba, D.; Ma, D.; Sun, S.; Govorov, A. O.; Zhao, H.; Wang, Z. M.; Rosei, F. Optoelectronic Properties in near-Infrared Colloidal Heterostructured Pyramidal "Giant" Core/Shell Quantum Dots. *Adv. Sci.* **2018**, *5*, 1800656.
(18) Selopal, G. S.; Zhao, H.; Wang, Z. M.; Rosei, F. Core/Shell Quantum Dots Solar Cells. *Adv. Funct. Mater.* **2020**, *30*, 1908762.
(19) Kobosko, S. M.; Jara, D. H.; Kamat, P. V. $AgInS_2$-ZnS Quantum Dots: Excited State Interactions with TiO_2 and Photovoltaic Performance. *ACS Appl. Mater. Interfaces* **2017**, *9*, 33379−33388.
(20) Kim, J. Y.; Jang, Y. J.; Park, J.; Kim, J.; Kang, J. S.; Chung, D. Y.; Sung, Y. E.; Lee, C.; Lee, J. S.; Ko, M. J. Highly Loaded PbS/Mn-Doped CdS Quantum Dots for Dual Application in Solar-to-Electrical and Solar-to-Chemical Energy Conversion. *Appl. Catal., B* **2018**, *227*, 409−417.
(21) Liu, G.; Liang, W.; Xue, X.; Rosei, F.; Wang, Y. Atomic Identification of Interfaces in Individual Core@Shell Quantum Dots. *Adv. Sci.* **2021**, *8*, 2102784.
(22) Zhang, J. Z.; Cooper, J. K.; Gul, S. Rational Codoping as a Strategy to Improve Optical Properties of Doped Semiconductor Quantum Dots. *J. Phys. Chem. Lett.* **2014**, *5*, 3694−3700.
(23) Sullivan, I.; Zoellner, B.; Maggard, P. A. Copper(I)-Based P-Type Oxides for Photoelectrochemical and Photovoltaic Solar Energy Conversion. *Chem. Mater.* **2016**, *28*, 5999−6016.
(24) Gawande, M. B.; Goswami, A.; Felpin, F. X.; Asefa, T.; Huang, X.; Silva, R.; Zou, X.; Zboril, R.; Varma, R. S. Cu and Cu-Based Nanoparticles: Synthesis and Applications in Catalysis. *Chem. Rev.* **2016**, *116*, 3722−3811.
(25) Karan, N. S.; Sarma, D. D.; Kadam, R. M.; Pradhan, N. Doping Transition Metal (Mn or Cu) Ions in Semiconductor Nanocrystals. *J. Phys. Chem. Lett.* **2010**, *1*, 2863−2866.
(26) Song, J.; Ma, C.; Zhang, W.; Li, X.; Zhang, W.; Wu, R.; Cheng, X.; Ali, A.; Yang, M.; Zhu, L.; Xia, R.; Xu, X. Bandgap and Structure Engineering Via Cation Exchange: From Binary Ag_2S to Ternary $AgInS_2$, Quaternary Agznins Alloy and AgZnInS/ZnS Core/Shell Fluorescent Nanocrystals for Bioimaging. *ACS Appl. Mater. Interfaces* **2016**, *8*, 24826−24836.
(27) Srivastava, B. B.; Jana, S.; Pradhan, N. Doping Cu in Semiconductor Nanocrystals: Some Old and Some New Physical Insights. *J. Am. Chem. Soc.* **2011**, *133*, 1007−1015.
(28) Brovelli, S.; Galland, C.; Viswanatha, R.; Klimov, V. I. Tuning Radiative Recombination in Cu-Doped Nanocrystals Via Electrochemical Control of Surface Trapping. *Nano Lett.* **2012**, *12*, 4372−4379.
(29) Jana, S.; Srivastava, B. B.; Acharya, S.; Santra, P. K.; Jana, N. R.; Sarma, D. D.; Pradhan, N. Prevention of Photooxidation in Blue-Green Emitting Cu Doped ZnSe Nanocrystals. *Chem. Commun.* **2010**, *46*, 2853−2855.
(30) Pradhan, N.; Goorskey, D.; Thessing, J.; Peng, X. An Alternative of CdSe Nanocrystal Emitters: Pure and Tunable Impurity Emissions in ZnSe Nanocrystals. *J. Am. Chem. Soc.* **2005**, *127*, 17586−17587.
(31) Whitham, P. J.; Knowles, K. E.; Reid, P. J.; Gamelin, D. R. Photoluminescence Blinking and Reversible Electron Trapping in Copper-Doped CdSe Nanocrystals. *Nano Lett.* **2015**, *15*, 4045−4051.
(32) Hughes, K. E.; Hartstein, K. H.; Gamelin, D. R. Photodoping and Transient Spectroscopies of Copper-Doped CdSe/CdS Nanocrystals. *ACS Nano* **2018**, *12*, 718−728.
(33) Yang, Z.; Fan, J. Z.; Proppe, A. H.; Arquer, F. P. G.; Rossouw, D.; Voznyy, O.; Lan, X.; Liu, M.; Walters, G.; Quintero-Bermudez, R.; Sun, B.; Hoogland, S.; Botton, G. A.; Kelley, S. O.; Sargent, E. H. Mixed-Quantum-Dot Solar Cells. *Nat. Commun.* **2017**, *8*, 1325.
(34) Guo, H.; Luo, B.; Wang, J.; Wang, B.; Huang, X.; Yang, J.; Gong, W.; Zhou, Y.; Niu, X. Boosting Photoelectrochemical Hydrogen Generation on Cu-Doped $AgIn_5S_8$/ZnS Colloidal Quantum Dot Sensitized Photoanodes Via Shell-Layer Homojunction Defect Passivation. *J. Mater. Chem. A* **2020**, *8*, 24655−24663.
(35) Kang, X.; Huang, L.; Yang, Y.; Pan, D. Scaling up the Aqueous Synthesis of Visible Light Emitting Multinary $AgInS_2$/ZnS Core/Shell Quantum Dots. *J. Phys. Chem. C* **2015**, *119*, 7933−7940.
(36) Zhong, H.; Lo, S. S.; Mirkovic, T.; Li, Y.; Ding, Y.; Li, Y.; Scholes, G. D. Noninjection Gram-Scale Synthesis of Monodisperse Pyramidal $CuInS_2$ Nanocrystals and Their Size-Dependent Properties. *ACS Nano* **2010**, *4*, 5253−5262.
(37) Liu, B.; Li, X.; Zhao, Q.; Ke, J.; Tadé, M.; Liu, S. Preparation of $AgInS_2/TiO_2$ Composites for Enhanced Photocatalytic Degradation of Gaseous O-Dichlorobenzene under Visible Light. *Appl. Catal., B* **2016**, *185*, 1−10.
(38) Jin, L.; Sirigu, G.; Tong, X.; Camellini, A.; Parisini, A.; Nicotra, G.; Spinella, C.; Zhao, H.; Sun, S.; Morandi, V.; Zavelani-Rossi, M.; Rosei, F.; Vomiero, A. Engineering Interfacial Structure in "Giant" PbS/CdS Quantum Dots for Photoelectrochemical Solar Energy Conversion. *Nano Energy* **2016**, *30*, 531−541.
(39) Zhou, Y.; Celikin, M.; Camellini, A.; Sirigu, G.; Tong, X.; Jin, L.; Basu, K.; Tong, X.; Barba, D.; Ma, D.; Sun, S.; Vidal, F.; Zavelani-Rossi, M.; Wang, Z. M.; Zhao, H.; Vomiero, A.; Rosei, F. Ultrasmall Nanoplatelets: The Ultimate Tuning of Optoelectronic Properties. *Adv. Energy Mater.* **2017**, *7*, 1602728.
(40) Colantoni, A.; Longo, L.; Boubaker, K. Structural Investigation of Photocatalyst Solid $Ag_{1-x}Cu_xInS_2$ Quaternary Alloys Sprayed Thin Films Optimized within the Lattice Compatibility Theory (Lct) Scope. *J. Mater.* **2014**, *2014*, 1−5.
(41) Luo, B.; Liu, J.; Guo, H.; Liu, X.; Song, R.; Shen, K.; Wang, Z. M.; Jing, D.; Selopal, G. S.; Rosei, F. High Efficiency Photoelectrochemical Hydrogen Generation Using Eco-Friendly Cu Doped Zn-in-Se Colloidal Quantum Dots. *Nano Energy* **2021**, *88*, 106220.
(42) Huang, D.; Persson, C. Photocatalyst $AgInS_2$ for Active Overall Water-Splitting: A First-Principles Study. *Chem. Phys. Lett.* **2014**, *591*, 189−192.
(43) Guo, H.; Liu, J.; Luo, B.; Huang, X.; Yang, J.; Chen, H.; Shi, L.; Liu, X.; Benetti, D.; Zhou, Y.; Selopal, G. S.; Rosei, F.; Wang, Z.; Niu, X. Unlocking the Effects of Cu Doping in Heavy-Metal-Free $AgIn_5S_8$ Quantum Dots for Highly Efficient Photoelectrochemical Solar Energy Conversion. *J. Mater. Chem. C* **2021**, *9*, 9610−9618.
(44) Park, Y. J.; Oh, J. H.; Han, N. S.; Yoon, H. C.; Park, S. M.; Do, Y. R.; Song, J. K. Photoluminescence of Band Gap States in $AgInS_2$ Nanoparticles. *J. Phys. Chem. C* **2014**, *118*, 25677−25683.
(45) Tong, X.; Kong, X. T.; Zhou, Y.; Navarro-Pardo, F.; Selopal, G. S.; Sun, S.; Govorov, A. O.; Zhao, H.; Wang, Z. M.; Rosei, F. Near-Infrared, Heavy Metal-Free Colloidal "Giant" Core/Shell Quantum Dots. *Adv. Energy Mater.* **2018**, *8*, 1701432.
(46) Robel, I.; Kuno, M.; Kamat, P. V. Size-Dependent Electron Injection from Excited Cdse Quantum Dots into TiO_2 Nanoparticles. *J. Am. Chem. Soc.* **2007**, *129*, 4136−4137.
(47) Adhikari, R.; Jin, L.; Navarro-Pardo, F.; Benetti, D.; AlOtaibi, B.; Vanka, S.; Zhao, H.; Mi, Z.; Vomiero, A.; Rosei, F. High Efficiency, Pt-Free Photoelectrochemical Cells for Solar Hydrogen Generation Based on "Giant" Quantum Dots. *Nano Energy* **2016**, *27*, 265−274.
(48) Zhang, H.; Besteiro, L. V.; Liu, J.; Wang, C.; Selopal, G. S.; Chen, Z.; Barba, D.; Wang, Z. M.; Zhao, H.; Lopinski, G. P.; Sun, S.; Rosei, F. Efficient and Stable Photoelectrochemical Hydrogen Generation Using Optimized Colloidal Heterostructured Quantum Dots. *Nano Energy* **2021**, *79*, 105416.
(49) Zhao, H.; Liu, J.; Vidal, F.; Vomiero, A.; Rosei, F. Tailoring the Interfacial Structure of Colloidal "Giant" Quantum Dots for Optoelectronic Applications. *Nanoscale* **2018**, *10*, 17189−17197.

https://doi.org/10.1021/acsomega.1c07045
ACS Omega 2022, 7, 9642−9651

(50) Kresse, G.; Joubert, D. From Ultrasoft Pseudopotentials to the Projector Augmented-Wave Method. *Phys. Rev. B* **1999**, *59*, 1758−1775.
(51) Kresse, G.; Furthmuller, J. Efficiency of Ab-Initio Total Energy Calculations for Metals and Semiconductors Using a Plane-Wave Basis Set - Sciencedirect. *Comput. Mater. Sci.* **1996**, *6*, 15−50.
(52) Kresse, G. G.; Furthmüller, J. J. Efficient Iterative Schemes for Ab Initio Total-Energy Calculations Using a Plane-Wave Basis Set. *Phys. Rev. B, Condensed matter.* **1996**, *54*, 11169.
(53) Perdew, J. P.; Burke, K.; Ernzerhof, M. Generalized Gradient Approximation Made Simple. *Phys. Rev. Lett.* **1996**, *77*, 3865−3868.
(54) Adamo, C.; Barone, V. Toward Reliable Density Functional Methods without Adjustable Parameters: The PBE0Model. *J. Chem. Phys.* **1999**, *110*, 6158−6170.
(55) Madsen, G. K. H.; Carrete, J.; Verstraete, M. J. BoltzTraP2, a Program for Interpolating Band Structures and Calculating Semi-Classical Transport Coefficients. *Comput. Phys. Commun.* **2018**, *231*, 140−145.

https://doi.org/10.1021/acsomega.1c07045
ACS Omega 2022, 7, 9642−9651